AIAA JOURNAL
Vol. 42, No. 11, November 2004

Separation Control on High Angle of Attack Airfoil Using Plasma Actuators

Martiqua L. Post* and Thomas C. Corke†
University of Notre Dame, Notre Dame, Indiana 46556

This work involves the documentation and control of leading-edge flow separation that occurs over an airfoil at high angles of attack, well above stall. A generic airfoil shape (NACA 66_3-018) was used because of its documented leading-edge stall characteristics. It was instrumented for surface-pressure measurements that were used to calculate lift coefficients. Mean-velocity profiles downstream of the airfoil were used to determine the drag coefficient. In addition to these, smoke streakline flow visualization was used to document the state of flow separation. The airfoil was operated over a range of freestream speeds from 10 to 30 m/s, giving chord Reynolds numbers from 77×10^3 to 333×10^3. Two types of plasma actuator designs were investigated. The first produced a spanwise array of streamwise vortices. The second produced a two-dimensional jet in the flow direction along the surface of the airfoil. The plasma actuators were found to lead to reattachment for angles of attack that were 8 deg past the stall angle (the highest investigated). This was accompanied by a full pressure recovery and up to a 400% increase in the lift-to-drag ratio.

Nomenclature

C_d	=	coefficient of drag
C_l	=	coefficient of lift
C_p	=	coefficient of pressure
c	=	chord
E	=	electric field strength
F_B	=	body force vector
H	=	total wake width
L/D	=	lift-to-drag ratio
P	=	local pressure
Re_c	=	chord Reynolds number
U	=	local velocity
V	=	voltage
x	=	distance in the x direction
α	=	angle of attack
ϵ_o	=	permittivity of free space
λ_D	=	Debye length
ρ	=	local fluid density
ϕ	=	local electric potential

Subscripts

max	=	maximum
s	=	static conditions
st	=	stall
∞	=	freestream conditions

Superscripts

L	=	lower surface of the airfoil
U	=	upper surface of the airfoil

Presented as Paper 2003-1024 at the 41st Aerospace Sciences Meeting, Reno, NV, 6–9 January 2003; received 6 June 2003; revision received 14 April 2004; accepted for publication 8 May 2004.

*Visiting Assistant Professor, Center for Flow Physics and Control, Aerospace and Mechanical Engineering Department. Member AIAA.

†Clark Chair Professor, Center for Flow Physics and Control, Aerospace and Mechanical Engineering Department. Associate Fellow AIAA.

Introduction

THE maximum lift and stall characteristics of a wing affect many performance aspects of aircraft including takeoff and landing distance, maximum and sustained turn rates, climb and glide rates, and flight ceiling.[1] In a two-dimensional wing, the lift at a given angle of attack can be increased by increasing camber. However, the maximum achievable lift is ultimately limited by the ability of the flow to follow the curvature of the airfoil. When it cannot, the flow separates. In some cases, this first occurs at the leading edge.

One solution to leading-edge separation is to increase the leading-edge radius. This is the principal effect of a leading-edge flap. An example is a Krueger flap, which consists of a hinged surface on the lower side of the wing leading edge that can extend out and ahead of the wing leading edge.

A slotted leading-edge flap (slat) is the leading-edge equivalent of a trailing-edge slotted flap. It works by allowing air from the high-pressure lower surface to flow to the upper surface to add momentum to the boundary layer and prevent flow separation.

Although these leading-edge devices are effective, they have some drawbacks. In particular, they are complicated, add weight to the wing, take volume from inside the wing when not in use, and are sources of airframe noise and vibration. Therefore, if they could be replaced by other flow-control devices, there could be a number of benefits.

Our approach to separation control on wings is based on the use of weakly ionized plasma actuators. These actuators consist of electrodes that are located on the airfoil surface. High-voltage ac supplied to the electrodes (~3–12 kV_{p-p}) causes the air in their vicinity to weakly ionize. The ionized air (plasma) in the presence of the electric-field gradient produced by the electrodes results in a body-force vector acting on the external flow that can induce steady or unsteady velocity components. Numerical simulations[2] of the electric field, body force, and induced velocities have led to optimized actuator designs. Descriptions of these designs were presented by Corke and Matlis[3] and Post.[4] Examples of different applications include exciting boundary-layer instabilities on a sharp cone at Mach 3.5 (Ref. 5), lift augmentation on a wing section,[6] wing-section leading-edge separation control, and separation control for blades in the low-pressure turbine stage of a turbojet engine.[7]

Our objective was to document leading-edge separation control using weakly ionized plasma actuators on generic airfoils at large angles of attack. These might be categorized as "plasma slats." The effectiveness of the actuator is based on flow visualization, pressure measurements on the surface of the airfoil from which we could

derive lift, and mean-velocity measurements in the wake of the airfoil from which we could derive drag. Parameters of interest are the configuration and optimum placement of the actuators and the minimum power requirements.

Experimental Setup

The experiment consisted of studying the ability to control leading-edge separation on a stationary airfoil at large angles of attack. It was conducted in one of the subsonic open-return wind tunnels in the Hessert Laboratory at Notre Dame. The test section is 0.61×0.61 m (2 ft^2) in cross section and 1.8 m (6 ft) in length. One side wall and the floor are clear to allow optical access for flow visualization. The back wall was used to mount an airfoil model. Probe access was through a slot in the ceiling. Probes were traversed using a two-directional traversing mechanism that was driven by computer-controlled stepper motors.

The airfoil used in the experiment was a NACA 66_3-018. This was chosen for a number of reasons. One was that it exhibits well-behaved leading-edge separation at high angles of attack. Another was that this airfoil had previously been used at Notre Dame with lift/drag measurements performed using a drag balance.[8] Because we were planning to infer lift and drag from surface-pressure measurements and wake profiles, this allowed us to make a direct comparison to benchmark our results.

Two airfoils with chord lengths 12.7 and 25.4 cm (5 and 10 in.) were used. The spanwise lengths of the airfoils were 25.4 cm (10 in.) and 39.4 cm (15.5 in.), respectively. The airfoils were cast in an epoxy-based polymer in two-piece molds.

The inside diameter of the pressure ports was 1.6 mm (0.0625 in.). A total of 29 surface pressure ports were used. The streamwise spacing between ports was relatively uniform around the airfoil. The ports were aligned in the flow direction at the half-span location of the airfoil. The pressure tubulations were connected to a scanning pressure valve that selectively connected each pressure port to a single pressure transducer.

End plates were mounted on the airfoils to minimize end effects. The end plates were made from clear Plexiglas to allow visual access for flow visualization over the surface of the airfoil. For the 12.7-cm (5-in.)-chord airfoil, the end plates were 35.6 cm (14 in.) long $\times$ 17.8 cm (7 in.) high $\times$ 3.2 mm (0.125 in.) thick. The leading and trailing ends of the end plates were cut to have an 8.9-cm (3.5-in.) radius. For the 25.4-cm (10-in.)-chord airfoil, the end plates were 40.6 cm (16 in.) $\times$ 20.2 cm (8 in.), with a 10.2-cm (4-in.) radius. The thickness was the same. Fig. 1 shows a schematic drawing for the smaller airfoil and a photograph of the outside of the tunnel test section.

The airfoils were mounted by passing the support tube through the back wall of the test section. The tube was held in place by a chuck that allowed angular motion for setting the angle of attack. The pressure tubes exited the tunnel through the support tube. The airfoils were centered in the spanwise direction in the tunnel test section.

A pitot static probe in the freestream was located at the entrance to the test section to monitor the freestream velocity U_∞ for the experiments. The static pressure from this probe was also used as the reference pressure for the pressure transducer.

A separate pitot static probe was mounted on the traversing mechanism. This was located at different positions downstream of the airfoil, on its spanwise centerline. Discrete points were sampled across the wake to determine the mean-velocity profile.

On the surface of the airfoil, the coefficient of pressure C_p was calculated as

$$C_p = \frac{P_s - P_\infty}{\frac{1}{2}\rho U_\infty^2} = \frac{P_s - P_\infty}{P_0 - P_\infty} \tag{1}$$

where P_s is the static pressure at each port, P_∞ is the static pressure of the freestream, ρ is the density of the freestream air, U_∞ is the velocity of the freestream, and P_0 is the total pressure of the freestream. The uncertainty in all of the coefficient of pressure data is 1.7%.

The coefficient of lift C_l is found by integrating the C_p distribution around the airfoil. The x/c locations of the pressure ports are the same on the upper and lower surfaces, so that

$$C_l = \int_0^1 \left(C_p^U - C_p^L\right) \mathrm{d}\left(\frac{x}{c}\right) \tag{2}$$

where the superscripts refer to the upper (U) and lower (L) surfaces of the airfoil. The uncertainty in all of the coefficient of lift data is 1.9%.

The drag coefficient C_d on the airfoil was determined from the mean-velocity profiles taken in the wake. This is given as

$$C_d = \frac{4}{U_\infty^2} \int_0^1 U(y)(U_\infty - U(y))\mathrm{d}\left(\frac{y}{H}\right) \tag{3}$$

where $U(y)$ is the local mean streamwise velocity and H is a distance that encompasses the full wake. The percent uncertainty in all of the coefficient of drag data is 9%. The velocity profiles used to determine the drag were measured well downstream of any recirculation region that might exist in the separated flow at high angles of attack. The location was typically two chord lengths downstream of the trailing edge.

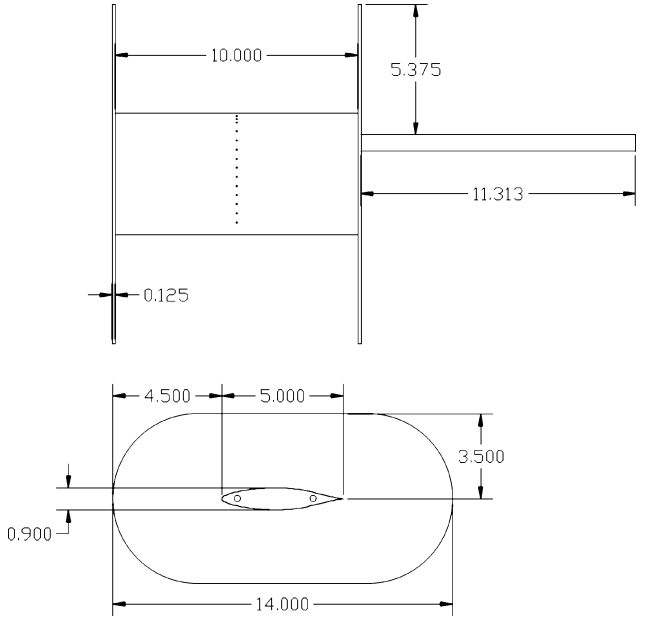

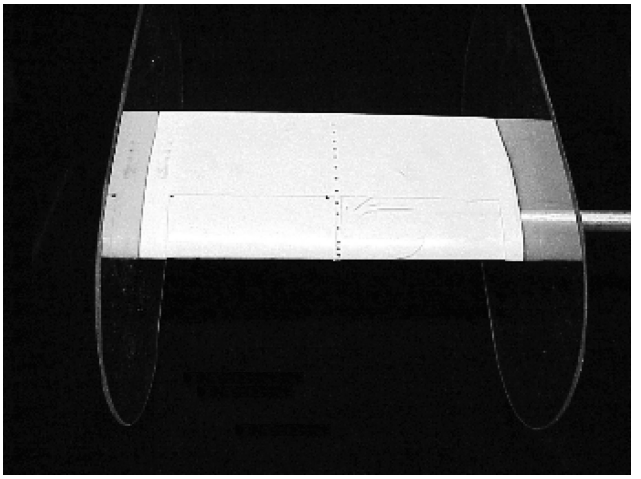

Fig. 1 Schematic drawing and photograph of 12.7-cm (5-in.)-chord airfoil with end plates. Dimensions are in inches.

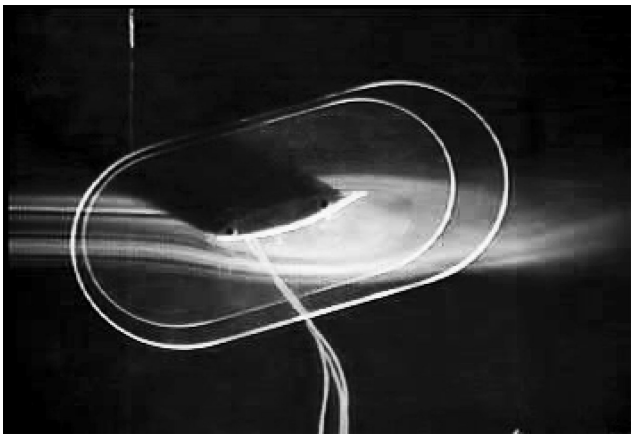

Fig. 2 Sample flow-visualization image for 12.7-cm (5-in.)-chord airfoil at 16-deg angle of attack and a freestream speed of 20 m/s (65.9 ft/s).

Flow visualization was done by introducing continuous smoke streaklines upstream of the wind-tunnel screens and contraction. A description of the smoke generator is given by Mueller.[9] The smoke emanated from a rake of tubes as low-speed laminar jets. The tubes were aligned in the vertical direction and located at the spanwise centerline. The smoke streaks were drawn into the tunnel inlet and converged into a closely spaced, vertically aligned group following the contraction.

The smoke streaks were illuminated with a steady high-intensity light source that was located below the tunnel test section. The light entered through a clear panel in the floor of the test section. The panel was covered except for a narrow slit so that the light would illuminate only the center portion of the airfoil. To visualize the separation region with the light entering from below, the symmetric airfoil was placed at negative angles of attack.

The visualized flow was recorded with a video camera onto analog videotape. The videotape was digitized through a video capture card, where individual frames could be extracted. An example of a flow-visualization image is shown in Fig. 2. In this arrangement, flow visualization was possible for freestream speeds up to 30 m/s.

Three freestream speeds of 10, 20, and 30 m/s were used. For the two chord lengths these gave a range of Reynolds numbers from 77×10^3 to 460×10^3.

Results

Baseline Conditions

The objectives of the baseline measurements were to document the angle of attack characteristics of the airfoil in our experiment and to benchmark the lift-coefficient measurements derived from the integrated C_p distributions against those made by Jansen[8] using a lift/drag balance. An example of a C_p distribution obtained in the experiment at $\alpha = 8$ deg at $Re_c = 75 \times 10^3$ is shown in Fig. 3. This Reynolds number corresponds to that of Jansen, for which we will compare the integrated C_p distribution to lift coefficients. This comparison is presented in Fig. 4 for angles of attack up to 16 deg. At this low Reynolds number, the linear C_l-vs-α region is not well defined. However, we still find reasonably good agreement between the two experiments.

A similar comparison at a higher Reynolds number of 200×10^3 is shown in Fig. 5. Here the linear C_l-vs-α region is very evident. We agree reasonably well with the previous lift-balance measurements in this regime. However, at higher angles of attack, Jansen[8] measured a higher maximum lift coefficient and stall angle, α_{st}. In our data, we observe a more relaxed stall regime which begins at α_{st} between 10 and 11 deg.

Baseline Vortex Generators

As a precursor to separation control using the plasma actuators, we investigated a common passive approach consisting of vortex generators. The vortex generators consisted of brass shim material

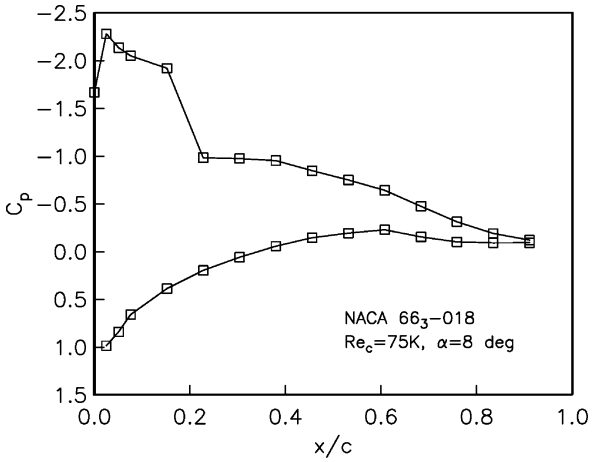

Fig. 3 Sample C_p distribution around airfoil for $\alpha = 8$ deg and $Re_c = 75 \times 10^3$. Uncertainty in C_p is 1.7% and in α is 2%.

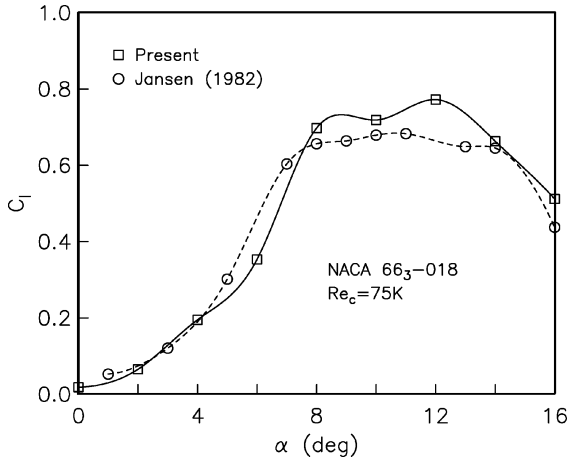

Fig. 4 Comparison between present lift-coefficient values found by integrating C_p distribution and those of Jansen[8] found using a lift balance at $Re_c = 75 \times 10^3$. Uncertainty in C_l for our data is 1.9%.

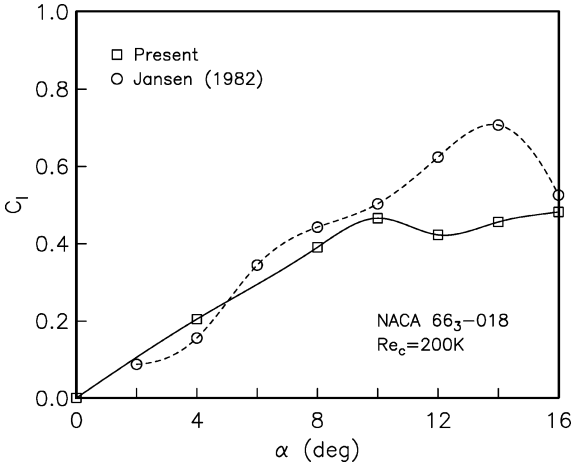

Fig. 5 Comparison between present lift-coefficient values found by integrating C_p distribution and those of Jansen[8] found using a lift-balance at $Re_c = 200 \times 10^3$. Uncertainty in C_l for our data is 1.9%.

that was bent at a 90-deg angle. A photograph of the vortex generators on the 12.7-cm (5-in.)-chord airfoil is shown in Fig. 6. The part of the vortex generator that is above the surface is approximately 2 mm square. This is estimated to extend past the edge of the boundary layer in the attached flow but is well within the separated-flow region at large angles of attack. The flat faces of the generators were oriented to be at 45 deg to the mean flow direction. The result would produce an array of corotating vortices.

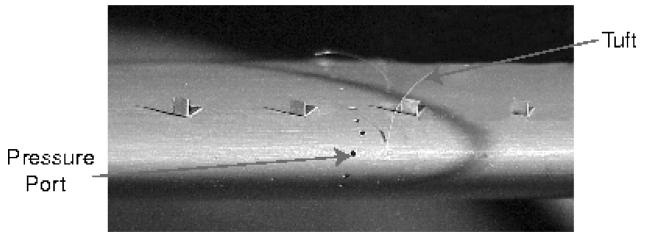

Fig. 6 Photograph of vortex generators used as a baseline flow-reattachment device on 12.7-cm (5-in.)-chord airfoil.

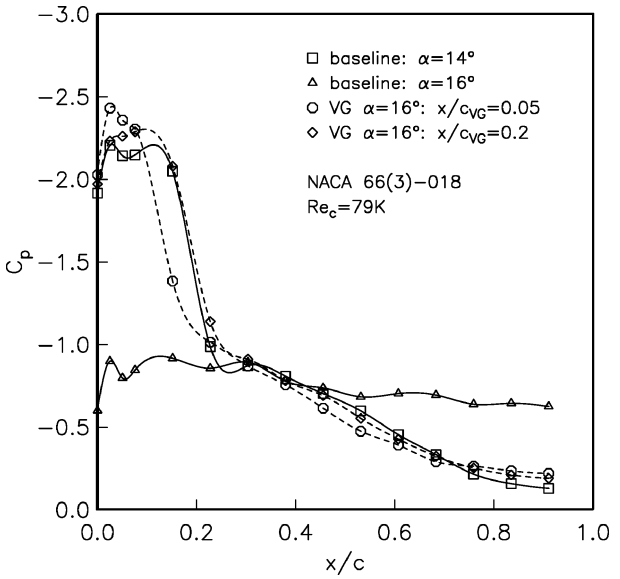

Fig. 7 Comparison of C_p distributions for pre- and poststall angles of attack without and with vortex generator tabs at $Re_c = 79 \times 10^3$. Uncertainty in C_p is 1.7%.

The effect of the vortex generators was documented for two angles of attack; the first near $C_{l_{\max}}$ and the other well past stall, where the flow was separating at the leading edge. Figure 7 documents the results at $Re_c = 79 \times 10^3$, corresponding to $U_\infty = 10$ m/s for the 12.7-cm (5-in.)-chord airfoil. This shows the C_p distribution around the airfoil. The baseline condition corresponds to the two angles of attack: at $C_{l_{\max}}$ ($\alpha = 14$ deg) and poststall ($\alpha = 16$ deg) without the vortex generators. Poststall, we observe a large decrease in the pressure on the suction side of the airfoil near the leading edge, which indicates a leading-edge separation.

The dashed curves in Fig. 7 show the C_p distributions with the vortex generators at two different x/c locations of 0.05 or 0.2. At both locations, the vortex generators are able to cause the flow to reattach, which is signified by recovery of the suction pressure near the leading edge. The vortex generators placed closer to the leading edge produced a higher $-C_p$ peak; however, those placed at $x/c = 0.2$ improved the suction pressure over a larger portion of the chord, so that the integrated effect was larger. Other measurements with the vortex generators at 30 m/s ($Re_c = 237 \times 10^3$) showed similar results, although the vortex generators located closer to the leading edge were slightly more effective overall.

Plasma Actuators

The plasma actuators consist of two metal electrodes that are separated by a dielectric insulator. A high-voltage ac input ($\sim$3–12 kV_{p-p}) is supplied to the electrodes. A schematic of the circuit used to generate the plasma is shown in Fig. 8. The first amplifier has variable gain. It was built using low-power operational amplifiers. The circuit was also designed to be able to produce a 180-deg. phase shift of the input signal. The next amplifier stage is designed to increase the output power to a level sufficient to drive the step-up transformers. This is a solid-state, push–pull amplifier that consists of discrete transistors. The circuit has an output amplitude of up to ± 100 V_{p-p} and a power rating of approximately 150 W per channel. The final stage of the plasma generation circuit is a 120:1 step-up transformer. These transformers were specially designed for a maximum output voltage of 20 kV, with a center frequency of 8 kHz.

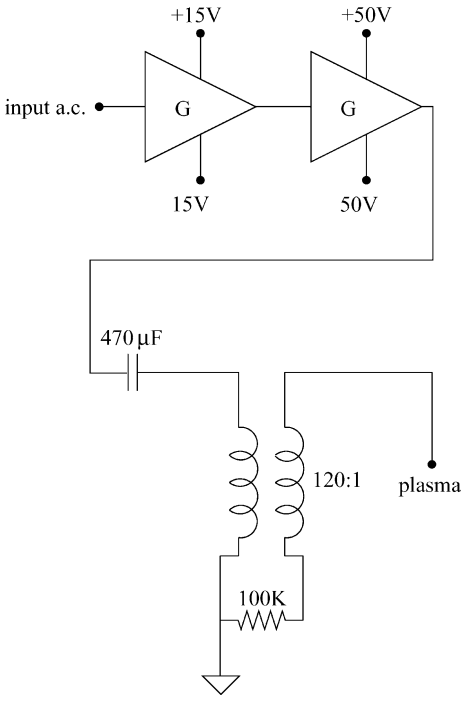

Fig. 8 Schematic of circuit used to generate the plasma.

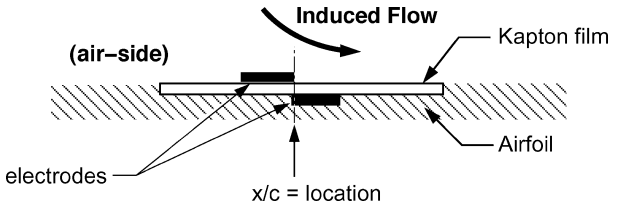

Fig. 9 Schematic drawing of asymmetric electrode arrangement for plasma actuators used in the experiments.

When the ac amplitude supplied to the electrodes is large enough, the air will ionize in the region of the highest electric potential. This is generally at the edge of the electrode that is exposed to the air. The ionized air, in the presence of an electric-field gradient, produces a body force on the ambient air.[10]

The body force per volume of plasma is a vector, given as

$$\boldsymbol{F}_B = \left(-\epsilon_0 / \lambda_D^2 \phi\right)\boldsymbol{E} \tag{4}$$

where ϵ_0 is the permittivity of free space, λ_D is the Debye length, ϕ is the electric potential, and $\boldsymbol{E}$ is the electric field vector, where

$$\boldsymbol{E} = -\nabla\phi \tag{5}$$

In one dimension, Eq. (1) reduces to

$$\boldsymbol{F}_B = (\epsilon_0/2)(\nabla E^2) \tag{6}$$

which we have used in the past to obtain an estimate of the body-force vector for use in the design of actuator-electrode arrangements. Post[4] demonstrated arrangements that could produce wall jets or spanwise or streamwise vortices when placed on the wall in a boundary layer.

Our approach to leading-edge separation control was to use an actuator having an asymmetric arrangement of electrodes such as shown in the schematic in Fig. 9. This results in a strongly asymmetric body force vector that produces a two-dimensional wall jet.

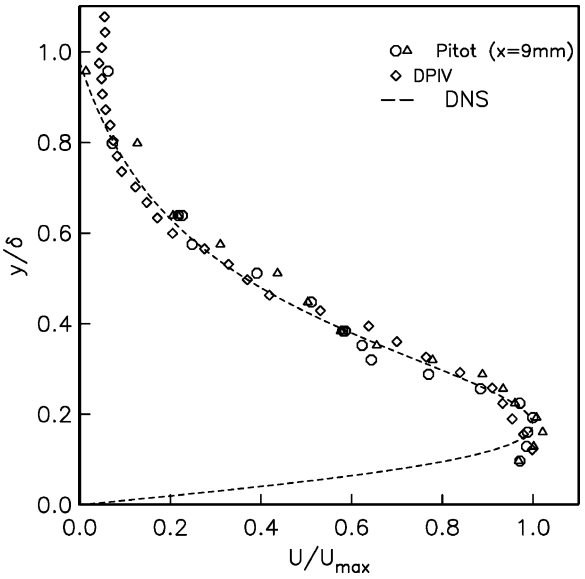

Fig. 10 Mean-velocity profile induced by an asymmetric plasma actuator similar to that used on the airfoil.

This is demonstrated in Fig. 10, which shows mean-velocity profiles on the downstream side of an actuator in an otherwise quiescent flow. The measurements were obtained using a particle image velocimetry (PIV) system and a traversing pitot probe. Also shown for comparison are the results from a direct numerical simulation (DNS) calculation for a plasma actuator in the arrangement in Fig. 9.

The electrodes are made from 0.0254-mm-thick copper-foil tape. They are separated by a dielectric layer. The dielectric material consisted of three layers of 0.0254-mm-thick Kapton film that were bonded together. The electrodes overlapped at one edge. The exact amount of overlap is not critical, although there needs to be some small amount (order of a millimeter) in order to have a uniform plasma in the full spanwise direction.

The sandwich arrangement of electrodes and dielectric layer was bonded to the surface of the airfoils. A recess equal to the thickness of the actuator had been added to the mold prior to casting the airfoils. When the actuator was added over the recessed area, a smooth flush surface is formed. Therefore, the addition of the actuator did not change the shape of the NACA 66_3-018 airfoil.

The ac voltage supplied to the electrodes was at a frequency of 5 kHz and was 11 kV in all cases unless otherwise specified. With regard to the flow, the effect can be considered to be steady, that is, a steady wall jet. We have the capability of producing unsteady effects at low frequencies (down to a fraction of a hertz if desired), but the results to follow were under steady conditions.

A number of plasma actuator arrangements have been investigated. One was an arrangement of electrodes that were designed to produce streamwise vortices similar to the vortex-generator tabs documented in the preceding section. However, the arrangement presented here is one that was designed to produce a steady two-dimensional wall jet in the flow direction and thereby add momentum to the boundary layer near the point of separation.

We have investigated the sensitivity of the placement of the actuators for the control of the leading-edge separation. In the results presented here two actuators were used. One was placed directly at the leading edge ($x/c = 0$) and oriented to produce a velocity component toward the suction side of the airfoil when at an angle of attack. The other was placed at the maximum-thickness location ($x/c = 0.5$) and oriented to produce a velocity component in the mean freestream direction. This is illustrated in Fig. 11.

Photographs of the airfoil with the electrodes and Kapton film in place are shown in Fig. 12. The space that was allotted for the actuator on the airfoil was relatively large to accommodate a variety of configurations. In the top photograph, most of the area is passive

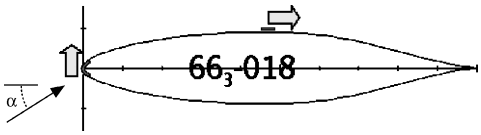

Fig. 11 Schematic drawing showing the locations and orientations of plasma actuators used for separation control.

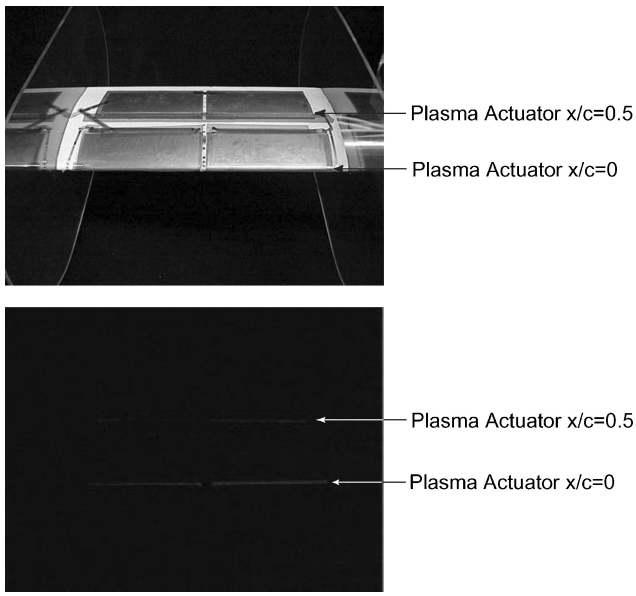

Fig. 12 Photographs of airfoil with plasma actuators at the leading-edge and midchord locations (top) and lines of plasma viewed in a darkened lab (bottom).

and covered by Kapton film to bring the recessed area flush with the other airfoil surface. The active actuator regions are best seen in the bottom photograph, which shows the two lines of plasma that are weakly visible at the leading edge and midchord locations when viewed in a darkened lab.

The actuator spanned most of the width of the airfoil. A narrow gap was left at the location of the pressure taps, although both sides were electrically connected.

Separation Control

The results in this section document the ability of the plasma actuators described in the preceding section to reattach the flow at high angles of attack. The first results are at a Reynolds number (79×10^3) comparable to that of which we examined the baseline vortex-generator tabs. Figure 13 shows an example of flow visualization without and with the plasma actuators on. Note again that the symmetric airfoil is at a negative angle of attack, so that the separated region is on the bottom, where the light source below the test section can illuminate that region.

In Fig. 13, $\alpha = 16$ deg, which is approximately 4 deg past α_s at $Re_c = 79 \times 10^3$. With the actuator off, the flow separates at the leading edge and forms a large recirculation bubble that extends beyond the trailing edge. With the actuator on, the flow is fully attached at the leading edge. The wake region is also visibly narrower, based on the number of smooth streak lines downstream of the airfoil. This will be quantified in the next results.

The suction-side C_p distributions for the conditions in the flow visualization in Fig. 13 are presented in Fig. 14. Included in Fig. 14 is the C_p distribution for the vortex-generator tab closest to the leading edge. We observe that the plasma actuator recovers the suction pressure better than the vortex generators.

Complete C_p distributions and mean-velocity profiles in the wake were used to determine the lift and drag coefficients for different angles of attack up to 18 deg, with the plasma actuator off and on. The results in terms of L/D are given in Table 1.

Table 1 Comparison of *L/D* with plasma actuators for $Re_c = 79 \times 10^3$

Actuator	α, deg	L/D
Off	16	14
On	16	60
Off	18	21
On	18	40

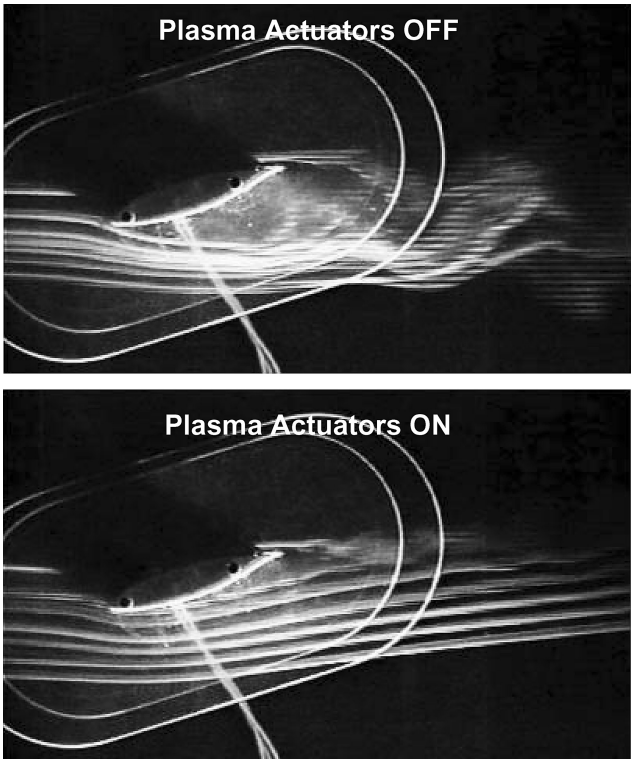

Fig. 13 Photographs of visualized flow around the airfoil with plasma actuator off (top) and on (bottom) for $\alpha = 16$ deg and $Re_c = 79 \times 10^3$.

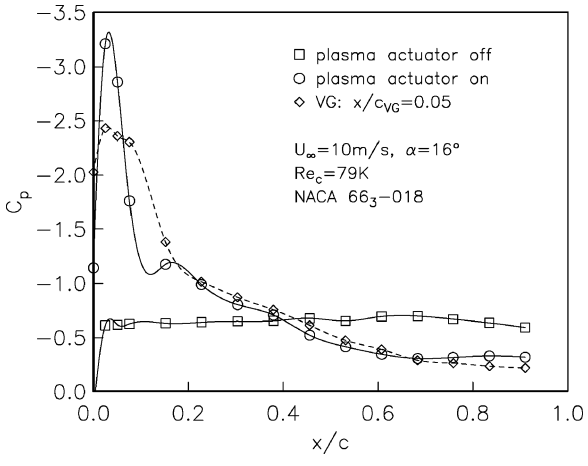

Fig. 14 Suction-side C_p distribution with the plasma actuator off and on and comparison to vortex generator for $\alpha = 16$ deg and $Re_c = 79 \times 10^3$. Uncertainty in C_p is 1.7%.

For the conditions in the flow visualization, the L/D ratio increased more than four times with the plasma actuator causing flow reattachment.

Figure 15 shows flow visualization with the plasma actuator off and on for a higher Re_c of 158×10^3. These are at the same $\alpha = 16$ deg as in Fig. 13, which is again approximately 4 deg past α_s. As before, the plasma actuator produces a fully attached leading-edge flow and a visibly narrower wake.

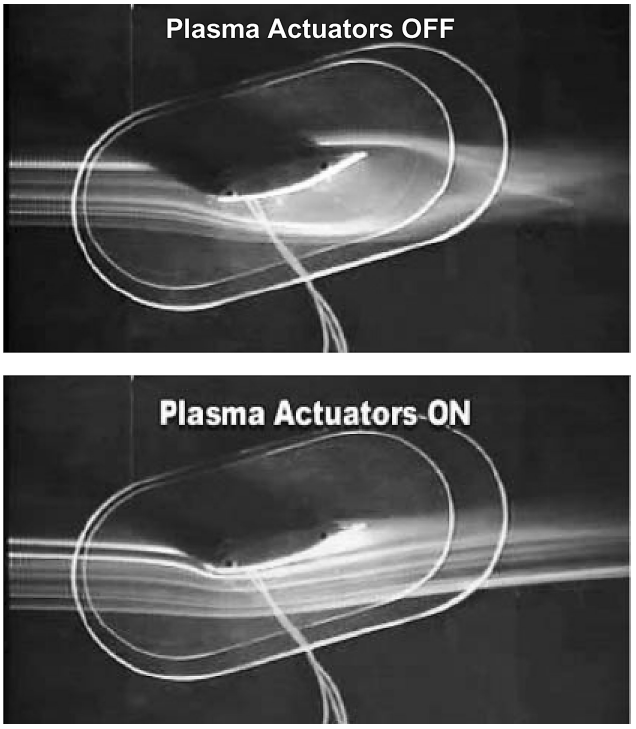

Fig. 15 Photographs of visualized flow around the airfoil with plasma actuator off (top) and on (bottom) for $\alpha = 16$ deg and $Re_c = 158 \times 10^3$.

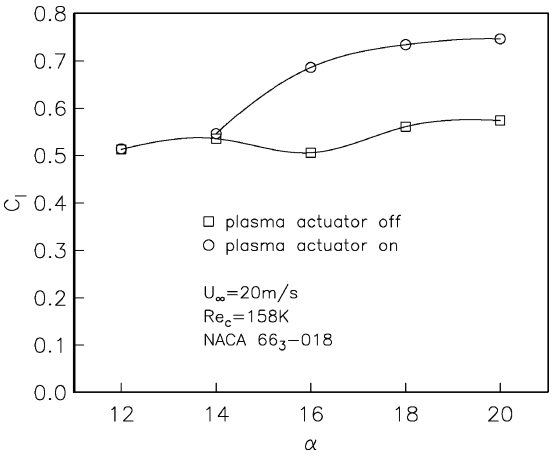

Fig. 16 Comparison of lift coefficient vs angle of attack with the plasma actuator off and on at $Re_c = 158 \times 10^3$. Uncertainty in C_l is 1.9% and in α is 2%.

The C_p distributions were similar to those at the lower Reynolds number (i.e., Fig. 14). Others were obtained for a range of angles of attack in order to determine the lift and drag coefficients. The results are presented in Figs. 16 and 17. These data are combined in the form of a drag polar, which is shown in Fig. 18. This demonstrates the significant performance enhancement of the airfoil that is produced by the plasma actuator.

All of the results to this point have been based on a single actuator amplitude (p–p voltage). This primarily relied on visual reattachment of the separated flow using flow visualization. The following considers the sensitivity of the lift and drag for the actuator amplitude.

Figures 19 and 20 document the effect of the plasma actuator amplitude on the C_p distributions on the suction side of the airfoil and the wake mean-velocity profiles. The amplitude designated as 100% corresponds to that used to obtain the previous results at $Re_c = 158 \times 10^3$, including the flow visualization in Fig. 15.

The C_p distributions in Fig. 19 indicate that essentially full pressure recovery occurred at 60% of the original amplitude and that

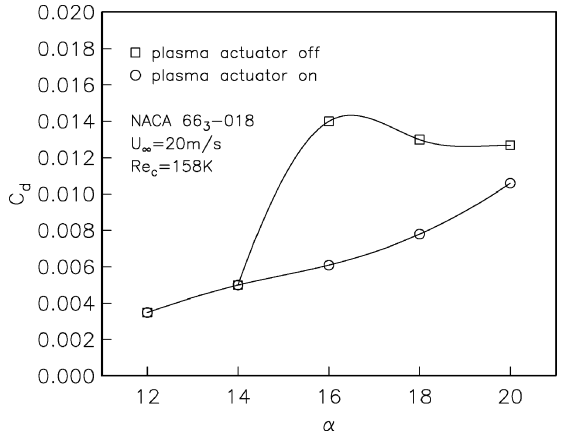

Fig. 17 Comparison of drag coefficient vs α with the plasma actuator off and on at $Re_c = 158 \times 10^3$. Uncertainty in C_d is 9% and in α is 2%.

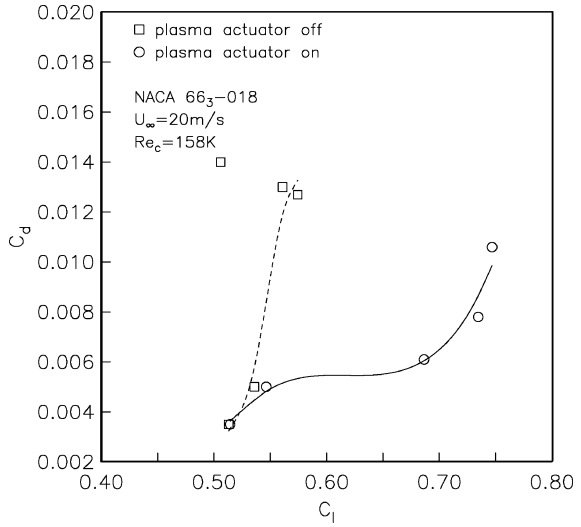

Fig. 18 Comparison of drag polars with the plasma actuator off and on at $Re_c = 158 \times 10^3$. Uncertainty in C_d is 9% and in C_l is 1.9%.

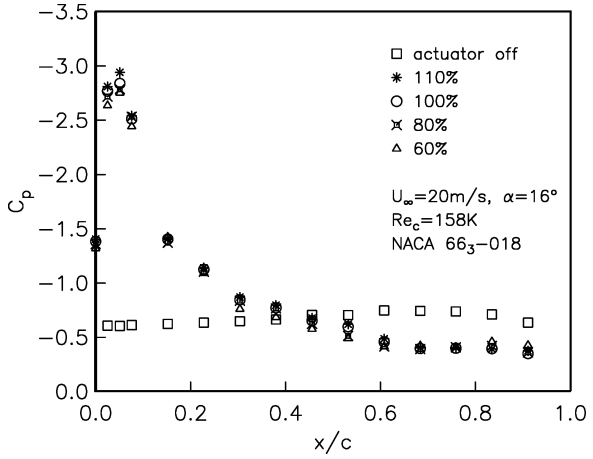

Fig. 19 Suction-side C_p distributions for different plasma-actuator amplitudes at $\alpha = 16$ deg and $Re_c = 158 \times 10^3$. Uncertainty in C_p is 1.7%.

there was minor improvement at higher amplitudes. In contrast, the wake profiles indicate sensitivity to the full range of actuator amplitudes with a trend to reduced drag as the amplitude increased.

Complete C_p distributions and mean-velocity profiles in the wake were used to determine the lift and drag coefficients for the different actuator amplitudes. These are plotted in Fig. 21, where the circle symbols correspond to C_l, which is read on the left axis, and the square symbols correspond to C_d, which is read on the right axis.

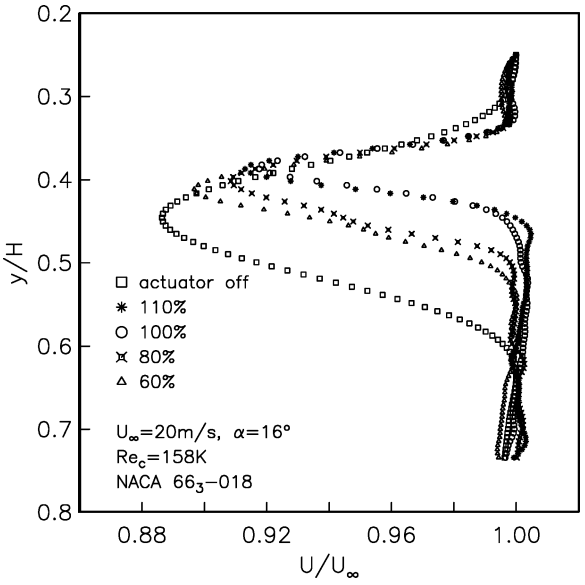

Fig. 20 Wake mean-velocity profiles for different plasma-actuator amplitudes at $\alpha = 16$ deg and $Re_c = 158 \times 10^3$. Uncertainties in U and y are each less than 1%.

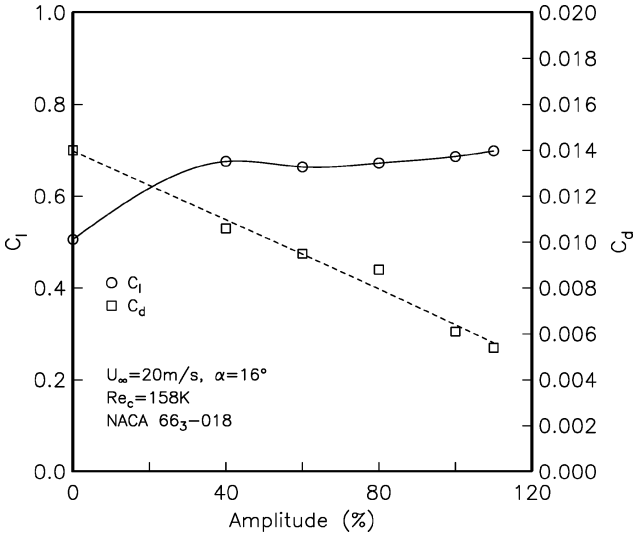

Fig. 21 Lift and drag coefficients for different plasma-actuator amplitudes at $\alpha = 16$ deg and $Re_c = 158 \times 10^3$. Uncertainty in C_d is 9% and in C_l is 1.9%.

The results in Fig. 21 indicate that for the lift coefficient, once a threshold amplitude was reached (approximately 40% in this case), the flow reattached, and there was little more to be gained in lift with additional actuator amplitude. However, for the drag coefficient, there was an approximately linear decrease in the drag as the actuator amplitude increased, even after the lift value had saturated. As a consequence, the L/D ratio continued to increase as the actuator amplitude increased. This decrease in drag is not attributed to any thrust produced by the actuator.

Our earlier work with leading-edge separation control using plasma actuators actually started with the larger chord airfoil. The focus shifted to the smaller chord because of concern with tunnel blockage at the large angles of attack we were able to achieve with the actuator. Nevertheless, this represents the highest-Reynolds-number conditions that we were able to document using flow visualization.

The initial work with the 25.4-cm (10-in.)-chord airfoils used four plasma actuators, which were equally spaced and started from the leading edge up to $x/c = 0.2$. The later work reported here has indicated that the most important actuator is the one at the leading edge. Therefore we speculate that in the earlier work, only the first

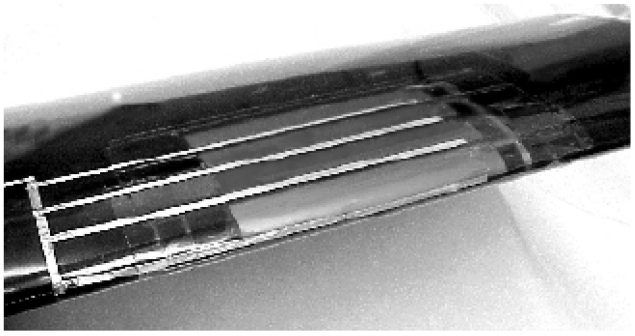

Fig. 22 Photograph of older actuator arrangement with four electrodes that was used with 25.4-cm (10-in.)-chord airfoil.

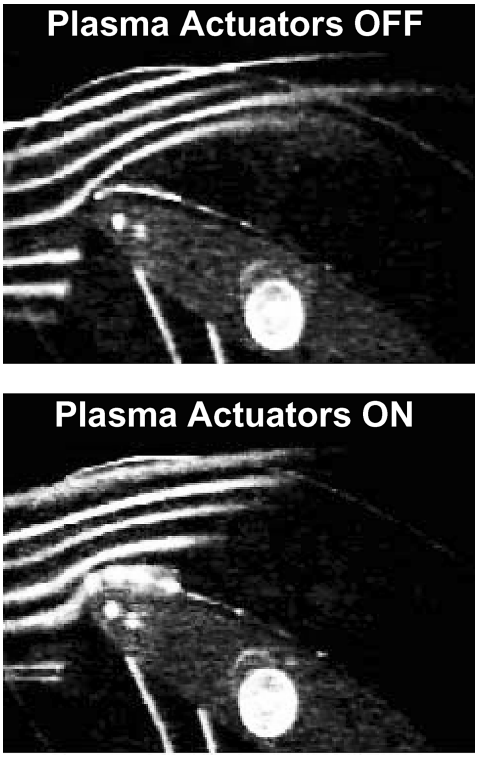

Fig. 23 Photograph of visualized flow over airfoil without (top) and with (bottom) plasma actuator on for $\alpha = 22$ deg and $Re_c = 333 \times 10^3$.

of the four actuators was required. The actuator design was similar in that they were aligned in the cross-flow direction and designed to add momentum in the mean flow direction, at the wall. Figure 22 shows a photograph of the actuator array on the airfoil.

A sample of the visualized flow without and with separation control is shown in Fig. 23. This corresponds to the 25.4-cm (10-in.)-chord airfoil at a freestream speed of 21 m/s, giving $Re_c = 333 \times 10^3$. In this case the light source was on the top of the test section. The airfoil was set at a positive angle of attack to illuminate the separated region on the upper surface. The angle of attack in these images is 22 deg (approximately 8 deg past stall).

With the actuator off, we observe a large separation region over the upper surface. With the actuator on, the smoke streak lines smoothly follow the leading edge, indicating that the flow has reattached. The lack of smoke over the downstream portion of the airfoil in these two pictures is due to the manner in which the light was introduced. This prompted the change to placing the light source below the test section, which was used in the flow visualization images presented earlier.

Summary

Weakly ionized plasma actuators were used to reattach leading-edge flow separation over a generic airfoil (NACA 66_3-018) for angles of attack of up to 8 deg past stall. This was documented for a range of velocities from 10 to 30 m/s and chord Reynolds numbers from 77×10^3 to 460×10^3.

The plasma actuator was designed to produce a steady two-dimensional wall jet in the flow direction and thereby add momentum to the boundary layer. Each actuator consisted of a pair of electrodes that were separated by a dielectric layer. The electrodes were in an asymmetric configuration that produced a body-force vector that would induce flow in one direction.

Two actuators were used. These were placed at the leading edge ($x/c = 0$) and at the maximum-thickness point on the airfoil ($x/c = 0.5$). Earlier work using four electrode pairs from $0 \leq x/c \leq 0.2$ indicated that the most effective actuator location to reattach the leading-edge flow separation was at the exact leading edge.

The lift was found by integrating the surface C_p distribution around the airfoil. This approach was found to agree well with measurements made with a lift balance.[8] The drag was found by calculating the momentum deficit in the wake based on measurements of the mean streamwise velocity profile.

The reattached flow produced by the actuator led to a significant suction-pressure recovery and drag reduction that yielded as much as a 400% increase in the L/D ratio. The estimated power to achieve this was approximately 20 W for the 25.4-cm airfoil span.

However, the results indicated that once a threshold amplitude was reached, the flow reattached, and there was little more to be gained in lift from additional actuator amplitude. The threshold amplitude was found to be approximately 40% of the power used for the bulk of the results. However, for the drag coefficient, there was an approximately linear decrease in the drag as the actuator amplitude increased, even after the lift value had saturated. As a consequence, the L/D ratio continued to increase as the actuator amplitude increased.

In terms of pressure recovery, we found results slightly better than yet comparable to those of vortex generator tabs. However, the advantage of the plasma actuators is that they can be operated only when needed, and when not in use, they produce no parasitic effects.

Acknowledgments

This work was supported by DARPA/ARO Grant DAAD19-00-1-0447, which was monitored by Richard Wlezien and Thomas Doligalski.

References

[1]Corke, T., *Design of Aircraft*, Prentice–Hall, New York, 2002.

[2]Enloe, L., McLaughlin, T., VanDyken, R., Kachner, Jumper, E., Corke, T., Post, M., and Haddad, O., "Mechanisms and Response of a Single Dielectric Barrier Plasma Actuator: Geometric Effects," *AIAA Journal*, Vol. 42, No. 3, 2004, pp. 595–604.

[3]Corke, T., and Matlis, E., "Phased Plasma Arrays for Unsteady Flow Control," AIAA Paper 2000-2323, Jan. 2000.

[4]Post, M. L., "Phased Plasma Actuators for Unsteady Flow Control," M.S. Thesis, Aerospace and Mechanical Engineering Dept., Univ. of Notre Dame, Notre Dame, IN, July 2001.

[5]Corke, T., Cavalieri, D., and Matlis, E., "Boundary Layer Instability on a Sharp Cone at Mach 3.5 with Controlled Input," *AIAA Journal*, Vol. 40, No. 5, 2002, pp. 1015–1018.

[6]Corke, T., Jumper, E., Post, M., Orlov, D., and McLaughlin, T., "Application of Weakly-Ionized Plasmas as Wing Flow-Control Devices," AIAA Paper 2002-0350, Jan. 2002.

[7]Huang, J., Corke, T., and Thomas, F., "Plasma Actuators for Separation Control of Low Pressure Turbine Blades," AIAA Paper 2003-1027, Jan. 2003.

[8]Jansen, B. J., Jr., "Experimental Studies of the Effect of the Laminar Separation Bubble on the Performance of a NACA 66_3-018 Airfoil at Low Reynolds Numbers," M.S. Thesis, Aerospace and Mechanical Engineering Dept., Univ. of Notre Dame, Notre Dame, IN, July 1982.

[9]Mueller, T. J., "On the Historical Development of Apparatus and Techniques for Smoke Visualization of Subsonic and Supersonic Flows," AIAA Paper 80-0420, 1980.

[10]Enloe, L., McLaughlin, T., VanDyken, R., Kachner, Jumper, E., and Corke, T., "Mechanisms and Response of a Single Dielectric Barrier Plasma Actuator: Plasma Morphology," *AIAA Journal*, Vol. 42, No. 3, 2004, pp. 589–594.

H. Reed
Associate Editor